MATERIALS SCIENCE

Autonomous self-healing optical sensors for damage intelligent soft-bodied systems

Hedan Bai[1]†, Young Seong Kim[1], Robert F. Shepherd[1,2]*

We introduce damage intelligent soft-bodied systems via a network of self-healing light guides for dynamic sensing (SHeaLDS). Exploiting the intrinsic damage resilience of light propagation in an optical waveguide, in combination with a tough, transparent, and autonomously self-healing polyurethane urea elastomer, SHeaLDS enables damage resilient and intelligent robots by self-healing cuts as well as detecting this damage and controlling the robot's actions accordingly. With optimized material and structural design for hyperelastic deformation of the robot and autonomous self-healing capacity, SHeaLDS provides reliable dynamic sensing at large strains (ε = 140%) with no drift or hysteresis, is resistant to punctures, and self-heals from cuts at room temperature with no external intervention. As a demonstration of utility, a soft quadruped protected by SHeaLDS detects and self-heals from extreme damage (e.g., six cuts on one leg) in 1 min and monitors and adapts its gait based on the damage condition autonomously through feedback control.

INTRODUCTION

The past two decades have seen proliferating growth in the maturing field of stretchable sensors. Using intrinsically soft materials or structurally compliant designs, stretchable sensors have demonstrated mechanically invisible monitoring of soft-bodied systems that are otherwise challenging for the silicon-based rigid counterparts (*1*–*4*). For sensing applications in damage-prone environments, intrinsically stretchable sensors constituted with elastomers are inherently damage resistant to blunt impacts (e.g., running over by a car), owing to the good toughness and resilience of elastomers (*5*–*8*); on the other hand, they are vulnerable to damage modes such as cuts and punctures. Incorporating self-healing properties into these intrinsically stretchable sensors promises not only damage-resistant but also damage-resilient sensing capabilities. Other than the immediately followed advantage of device longevity, self-healing stretchable sensors present a unique opportunity to establish damage intelligence into soft-bodied systems, similarly vulnerable to sharp damages. Examples range from damage detection in spacesuits to alert suit air leakage by space debris during astronauts' extravehicular activities (*9*) to robots that are not only resilient to damage *(10*–*12)* but also intelligent toward damage (i.e., able to detect the onset of damage and adapt through feedback control) when working in hazardous environments.

To enable damage intelligence, stretchable strain sensors need to (i) be tough and autonomously self-healable for both resistance and resilience toward damage and (ii) able to detect damage and provide reliable dynamic sensing performance (i.e., sensitivity, range, and bandwidth) for the intended strain sensing application (e.g., motion monitoring as robotic skins or wearables). The major challenge in building such a system is achieving a self-healing sensor that satisfies both requirements at the same time, and the challenge partially originates from the complexity of the self-healing material itself. Self-healing function for strain sensors comprises the recovery of material's mechanical properties and the restoration of sensing signals. Self-healing of polymers' mechanical properties has been realized through (i) extrinsic self-healing with healing reagents encapsulated in microcapsules (*13*, *14*) or fed through vascular networks (*15*) (ii) intrinsic self-healing by the reorganization of polymer chains and bonds at the damaged site with stimuli or autonomously without external energy input through dynamic bonding of supramolecular interactions or dynamic covalent chemistry (*16*–*19*). Among these mechanisms, intrinsic self-healing through dynamic bonding promises a simple embodiment as the basis of autonomous self-healing sensors. Incorporating conductive particulates in self-healing materials, self-healing of the sensing signals has been achieved through electrical sensing mechanisms [e.g., piezoresistive (*20*), ionic (*21*, *22*), or capacitive (*23*)] and has demonstrated quasi-static measurements (e.g., strain/flexion/pressure) (*24*). Few sensors, however, have been able to provide satisfactory sensing performance for dynamic strain measurements required in motion monitoring. Dynamic sensing with self-healing sensors usually exhibits large drift under continuous cyclic loading, hysteresis, heavy strain rate dependency, and limited strain range due to the intrinsic viscoelasticity from the dynamic bonding that enables self-healing. Sensors that are both autonomously self-healable and reliable in dynamic sensing have yet to be achieved.

We introduce an autonomous self-healing optical sensing mechanism, networks of self-healing light guides for dynamic sensing (SHeaLDS), which exploit the damage-resilient properties intrinsic to light propagation, in combination with an intrinsic self-healing material to achieve an optomechanical sensor that both autonomously self-heals and provides reliable dynamic sensing performance. Compared to electrical signals that require physical contact for transmission, light propagation in a waveguide through total internal reflection does not require mechanical contact. Therefore, the sensing signal (i.e., output light intensity) of a self-healing optical waveguide sensor is intrinsically resilient to damage and can be autonomously recovered not only when the

[1]Sibley School of Mechanical and Aerospace Engineering, Cornell University, Ithaca, NY 14850, USA. [2]Department of Materials Science and Engineering, Cornell University, Ithaca, NY 14850, USA .
*Corresponding author. Email: rfs247@cornell.edu
†Present address: Querrey Simpson Institute for Bioelectronics, Northwestern University, Evanston, IL 60208, USA.

damaged interfaces connect but also when small gaps remain (e.g., material removal through punctures). The self-healing function of the sensor is then simplified to self-healing the mechanical properties of the sensor material. To overcome the contradiction between autonomous self-healing and material viscoelasticity-driven sensor drift and hysteresis, we design SHeaLDS into a wavy shape that achieves good dynamic sensing through structural compliance. We demonstrate SHeaLDS′ fast and autonomous self-healing, damage detection, and dynamic sensing capabilities by integration onto self-sealing actuators to construct a soft quadruped that is intelligent about damage.

RESULTS

Autonomous self-healing polyurethane urea elastomer

Mechanical self-healing of SHeaLDS demands a material chemistry that fulfills the key requirements for damage intelligence. There are a myriad of chemistries for intrinsic self-healing elastomers with various properties (*16*, *17*, *25*). For this robotic application, some properties are especially useful: (i) For autonomous robots, the material needs to self-heal fast and autonomously without external assistance. (ii) It needs to be tough such that it cannot be easily damaged. (iii) As a material for optomechanical sensing, it needs to be transparent and elastic to deliver reliable measurements. Integrating this rigorous set of requirements into a self-healing polymer poses challenges in material design. Strategies toward tough and autonomous self-healing polymers have been demonstrated through (i) dynamic supramolecular approach that combines hydrogen bonds for self-healing and sacrificial noncovalent bonds for material toughening (*26*, *27*) and (ii) a strong dynamic covalent bond, the aromatic disulfide bond, that can undergo exchange reaction at room temperature (*28*–*32*).

Building on this knowledge, we report a self-healing polyurethane urea (sPUU) system that involves dynamic bonds with tiered bond strength to realize a tough and autonomous self-healing material that is also transparent and elastic (Fig. 1A and fig. S1). Specifically, sPUU is cross-linked with the strong yet dynamic aromatic disulfide bonds, which enable room-temperature self-healing to recover high strength. sPUU also has abundant hydrogen bonds from the urea and urethane groups, contributing to rapid and autonomous self-healing, as well as acting as sacrificial bonds for material toughening. Because these sacrificial bonds are also dynamic, the dissipated energy can be restored to enable tough yet elastic self-healing materials.

The resultant material (Figs. 1B and 2A and table S2) is an autonomously self-healable polyurethane (PU) urea that exhibits superior toughness (U_T = 60.6 MJ m^{-3}), high extensibility (ε_u = 1443%), high strength (σ_u = 7 MPa), and good optical transparency (*T*~80%). Cutting the sPUU exposes abundant reactive disulfide end groups and hydrogen bonds; as the damaged interfaces approach and adhere with confluent physical contact, polymer chains with those reactive end groups interdiffuse at the fresh interfaces (*33*), reforming disulfide and hydrogen bonds that effectively restore the material′s mechanical strength. We varied the polymer chain length to optimize material properties for use as optical sensors. As the polymer chain becomes longer with increasing polyol molecular weight (sPUU650, sPUU1000, and sPUU2000; fig. S1 and table S2), elasticity improves (i.e., glass transition temperature decreases; fig. S2 and table S1; creep test, fig. S3), while chain mobility decreases. sPUU1000 [poly(tetrahydrofuran) (PTMEG), M_n = 1000 g mol^{-1}] self-heals at room temperature and recovers to ε = 747% ($\frac{L-L_0}{L_0}^*$ 100, where *L* is the final length and L_0 is initial length; η = 52% defined by fracture strain) in 1 hour and ε = 1116% (η = 77%) in 24 hours (Fig. 1, C and E) sPUU 2000 (PTMEG, M_n = 2000 g mol^{-1}) recovers ε =158% (η = 15%) at room temperature and requires heating at 80°C for 1 hour to recover to ε = 970% (η = 84%) (Fig. 1D). sPUU2000 exhibits rapid autonomous self-healing, where after 1 min at room temperature, it can recover to ε = 23% and σ = 256 kPa. At both room temperature and 40°C in 1 hour (Fig. 1F), sPUU2000 self-heals to ε ~ 100% (η ~ 10%). Self-healing efficiency greatly increases for elevated temperatures close to 60°C, where sPUU2000 recovers to ε =450% (η = 40%) at 60°C and ε ~ 970% (η ~ 84%) at 80°C in 1 hour. At room temperature, however, even with 24 days′ healing time (Fig. 1D), sPUU2000 could only self-heal to ε ~ 100% (η ~ 10%). The self-healing efficiency at different temperatures suggests a topology freezing transition temperature (T_v) of sPUU2000 between 40° and 60°C, where the sPUU2000 exhibits vitrimetric property of transiting from an elastic solid to a viscoelastic liquid above T_v (*34*). On the other hand, sPUU1000 shows increased self-healing efficiency with prolonged healing time at room temperature (Fig. 1C), suggesting T_v for sPUU1000 is below room temperature. Above T_v, polymer flow allows rapid bond exchange reactions that are otherwise suppressed at $T < T_v$; at $T > T_v$, higher temperature leads to higher self-healing efficiency with the same healing time. This effect also agrees with the radical-mediated mechanism of disulfide exchange reaction that is influenced by chain mobility (note S1). We chose sPUU2000 as the optical sensor material to optimize both material elasticity and self-healing performance in the range of ε < 100% for our soft robotic application.

To investigate the robustness of self-healing ability in real-world scenarios, we characterized sPUU2000′s self-healing performance in two adverse damage conditions possible in robotic applications: damage that produces rough severed interfaces and damage that exposes the severed surfaces to age for prolonged time before reconnection. We created rough damage surfaces using a hand saw to demonstrate a possible real-world damage mode. Images of the damaged interfaces (fig. S4) qualitatively compare the smooth surface of a clean cut by a razor blade with the rough surface produced by a hand saw. Upon reconnection and resting for 1 hour, self-healing efficiency of the rough surface sample deteriorates compared to the clean cut due to compromised surface contact (Fig. 1G). The rough surface sample, however, can still self-heal to ε = 104% (η = 9%) at room temperature and ε = 742% (η = 65%) at 120°C in 1 hour. Self-healing capacity preserves despite lower efficiency for a hand-sawed rough damage interface.

It is well known that surface aging could incapacitate self-healing when the functional end groups at the damaged interface react with moisture or oxygen in the air [e.g., saturation of hydrogen bonding (*26*, *35*)]. To investigate surface aging effect on self-healing performance of our material, we cut sPUU2000 samples and exposed the damaged interfaces in air at room temperature for 5 min, 2, 24, and 48 hours before reconnection and allowed 1-hour self-healing time at room temperature. As shown in Fig. 1H, prolonged aging time did not deteriorate self-healing efficiency, where sPUU2000 samples aged for 5 min to 48 hours all self-healed to ε ~ 90% (η ~ 8%) in 1 hour at room temperature. Even with 48 hours′ surface aging, sPUU2000 can still self-heal to ε ~ 800% (η ~ 70%)

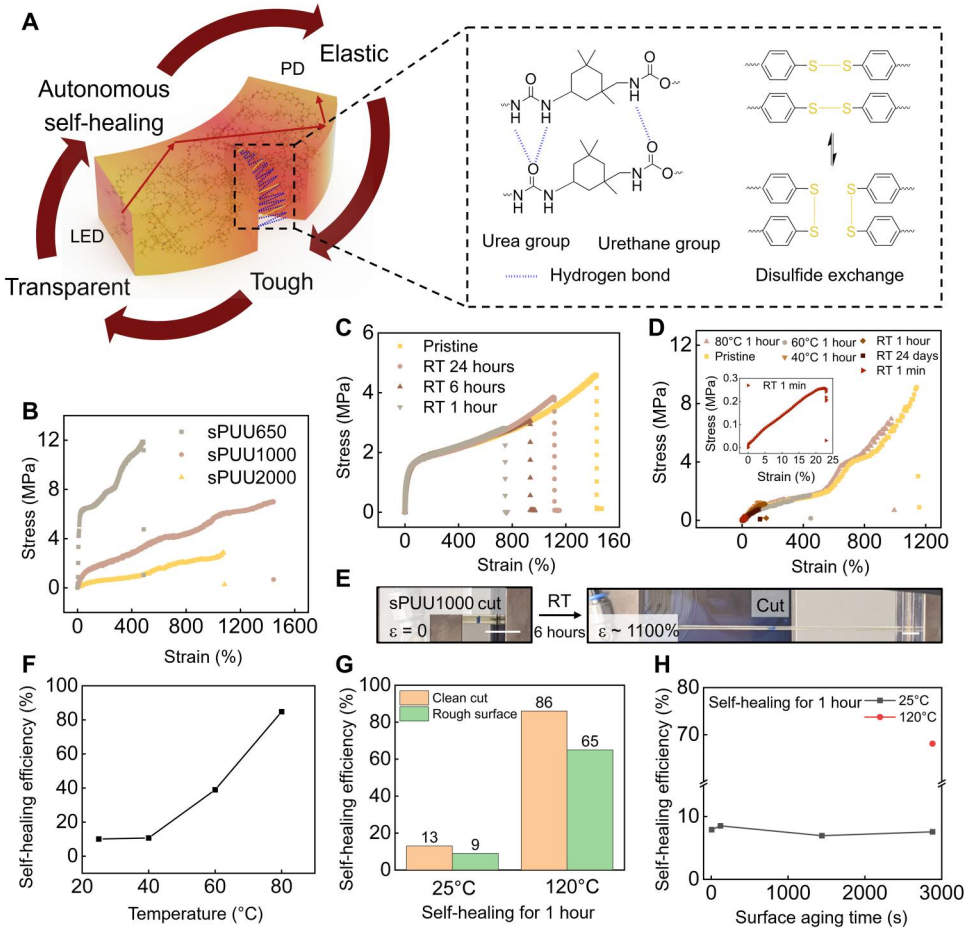

Fig. 1. Self-healing material design and mechanical self-healing properties. (**A**) Schematic illustration of the sPUU elastomer and integration as an optical waveguide sensor supporting ray propagation. Self-healing of sPUU is achieved through the combination of noncovalent interaction of hydrogen bond and dynamic covalent interaction of disulfide exchange. LED, light-emitting diode; PD, photodiode. (**B**) Stress-strain curves of sPUUs showing decreasing elastic modulus with increasing PTMEG molecular weight. Strain rates are 100 mm min^{-1}. (**C**) Stress-strain curves of sPUU1000 self-healed in room temperature (RT) for different periods of time. Strain rates are 60 mm min^{-1}. (**D**) Stress-strain curves of sPUU2000 self-healed in room temperature and elevated temperatures for different periods of time. Pristine sample fractures at ε = 1150% ($\frac{L-L_0}{L_0}^*$ 100). Strain rates are 500 mm min^{-1}. The strain hardening effect around 600% strain is caused by an artifact in the loading condition: Inadvertent jump in strain rate leads to temporary strain hardening, as expected from viscoelastic materials. Variation of material modulus for the same material formulation in (B) to (D) results from characteristic stress-strain response of viscoelastic materials that is strain rate dependent. (**E**) sPUU1000 with one cut can stretch to ε ~ 1100% after self-healing at room temperature for 6 hours. Scale bars, 5 mm. (**F**). Self-healing efficiency of sPUU2000 after healing for 1 hour at different temperatures. (**G**) Comparison of sPUU2000's self-healing efficiency between a smooth damage interface (clean cut by razor blade) and a rough damage surface (by hand saw). (**H**) Self-healing efficiency of sPUU2000 with variable surface aging time (self-healing condition: 1 hour at 25° and 120°C).

in 1 hour at 120°C. We further immersed the freshly cut samples in tap water for 10 min to expose the severed interfaces with abundant water molecules and then reconnect them to allow self-healing for 1 hour at different temperatures. Figure S5 shows self-healing efficiency deteriorates compared to samples with no surface aging; on the other hand, even after the severed surfaces are exposed to and aged in water, sPUU2000 could still self-heal to ε ~ 70% (η ~ 6%) in 1 hour at room temperature and to ε ~ 900% (η ~ 80%) in 1 hour at 120°C. This indicates that despite water may have partially caused saturation and dissociation of hydrogen bonds in the material, most of the self-healing capacity is preserved. The retained self-healing ability may be attributed to (i) hydrogen bonds remaining associated in the self-healing material due to the hydrophobic PU backbone (*27*) and (ii) disulfide exchange reaction insensitive to water (*36*).

Mechanism of self-healing optomechanical sensor

As shown in several prior works (*37*–*39*), the optomechanical sensing principle is based on optical path variation of the total internal-reflected rays in a light guide as it is deformed. When SHeaLDS are cut by a razor blade (Fig. 2B), output intensity temporarily drops to zero due to the blockage of the propagating rays, detecting the onset of a cut; lateral alignment and connection of the broken pieces immediately restore the output intensity with little loss (Fig. 2C). This coupling loss could be very low as light travels across a boundary between two mediums with the same refractive index ($n_1 = n_2$), reflected light intensity is zero [reflectance $R = \left(\frac{n_1-n_2}{n_1+n_2}\right)^2$] (*40*). Most of the loss comes from misalignment, and the coupling efficiency is the ratio of the overlapping area to the light guide core area (*40*); partial loss can also arise from light

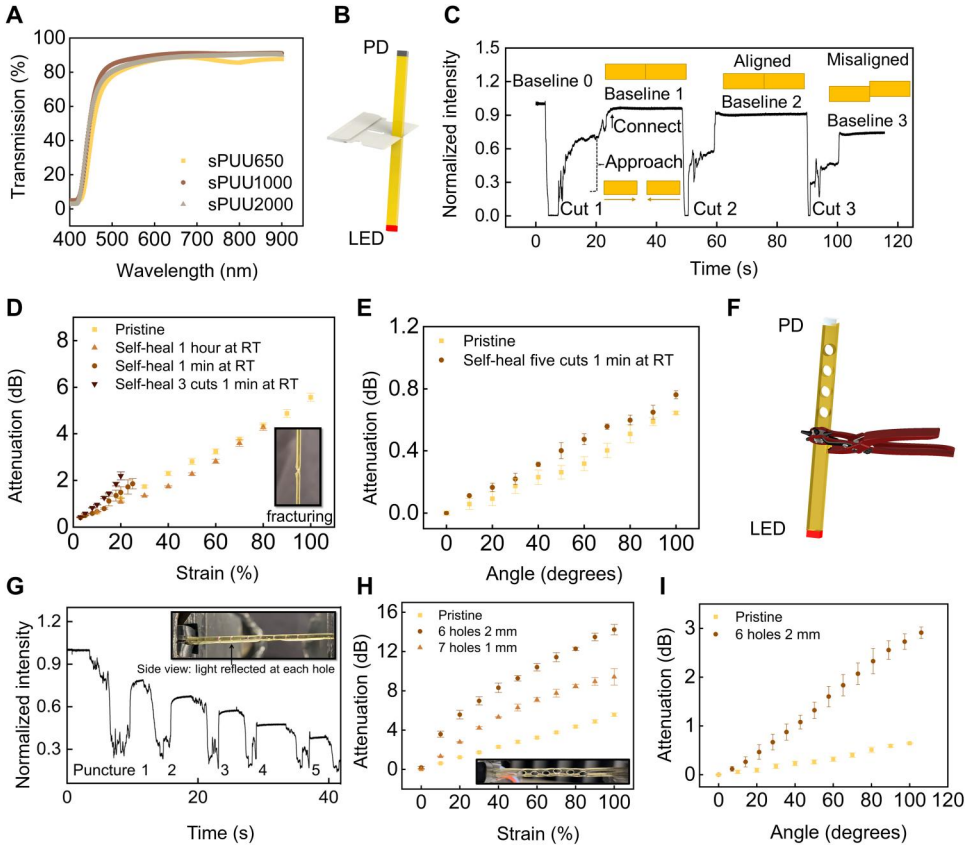

Fig. 2. Optical properties of sPUU and characterization of straight optical waveguide sensor for autonomously self-healing elongation and flexion sensing. (**A**) Transmission spectrum of sPUUs with 1.5-mm film thickness. All sPUUs exhibit over 80% transmission for 500- to 900-nm wavelength range. (**B**) Schematics of SHeaLDS cut by a razor blade. Not drawn to scale. (**C**) Real-time sensor response to cuts. Output intensity decreases to close to zero at each cut, partially recovers as the severed interfaces approach, and largely recovers as the two severed surfaces connect with a decreased baseline intensity, which depends on the quality of the alignment. (**D**) Room temperature self-healing sensor response to strain. Inset: Photograph of a cut site fracturing, which introduces increased attenuation at close-to-fracture strains. (**E**) Sensor response to bending after self-healing from five cuts for 1 min in room temperature. (**F**) Schematics of SHeaLDS punctured with material removal. Not drawn to scale. (**G**) Realtime sensor response to punctures. Output intensity decreases to close to zero at each puncture and recovers with partial loss from light reflection and bifurcation. Inset: Photograph of light reflecting at each hole. (**H**) Sensor response to strain with hole punctures. Inset: Photograph of six punctures of 2-mm-diameter holes. (**I**) Sensor response to bending after six punctures of 2-mm-diameter holes. More severe material removal leads to increased strain and flexion sensitivity as the waveguide becomes more lossy.

scattering due to surface roughness. As a strain sensor, SHeaLDS autonomously recovers sensing to $\varepsilon \sim 80\%$ in 1 hour, and measurements match that of the pristine state with a sensitivity of 5.3 dB ε^{-1}; self-healing for 1 min, SHeaLDS recovers over $\varepsilon \sim 20\%$ sensing with an increased sensitivity at $\varepsilon \sim 20\%$ due to increased optical loss at the near fracture state (Fig. 2D). As a flexion sensor, SHeaLDS chopped into five pieces autonomously recovers bend sensing to 100° after 1 min with measurements closely resembling that of the pristine state (Fig. 2E).

Enabled by the intrinsic damage resilience of the optical sensing mechanism and the high toughness of the self-healing material, SHeaLDS is robust from substantial material removal. Similar to cuts, SHeaLDS detects punctures (Fig. 2F) by output intensity decrease past a threshold; output resumes immediately with optical loss from the voids (Fig. 2G). Puncture creates a new boundary of air and the sensor medium, resulting in reflectance at the interface; as light rays enter the voids ($n_2 = 1$) from the light guide ($n_1 = 1.52$), beam divergence prevents some rays to be intercepted by the following light guide section. Compared to the pristine state, the more materials removed, the more sensitive SHeaLDS become at strain and flexion measurements, because voids render them more lossy waveguides. SHeaLDS punctured with six holes, each removing ~62% of the waveguide width, can still repeatedly measure strain to $\varepsilon \sim 100\%$ with a sensitivity of 14.23 dB ε^{-1} (Fig. 2H) and bend to 100° (Fig. 2I and movie S3), both with increased sensitivity than the pristine states.

Structural compliance for dynamic self-healing sensing

Despite the repeatable strain measurements in quasi-static sensing, dynamic strain measurement with SHeaLDS still suffers from viscoelasticity of the self-healing material. During the unloading process of each cyclic loading, SHeaLDS experiences a sudden signal drop followed by a slow signal recovery (Fig. 3A). We attribute this response to the viscoelasticity of the self-healing material, where SHeaLDs buckles at the time scale of the load removal and straightens to the undeformed state with a recovery time. The recovery time lengthens with slower strain rate and higher maximum strain reached (fig. S6). For dynamic sensing, this behavior means large

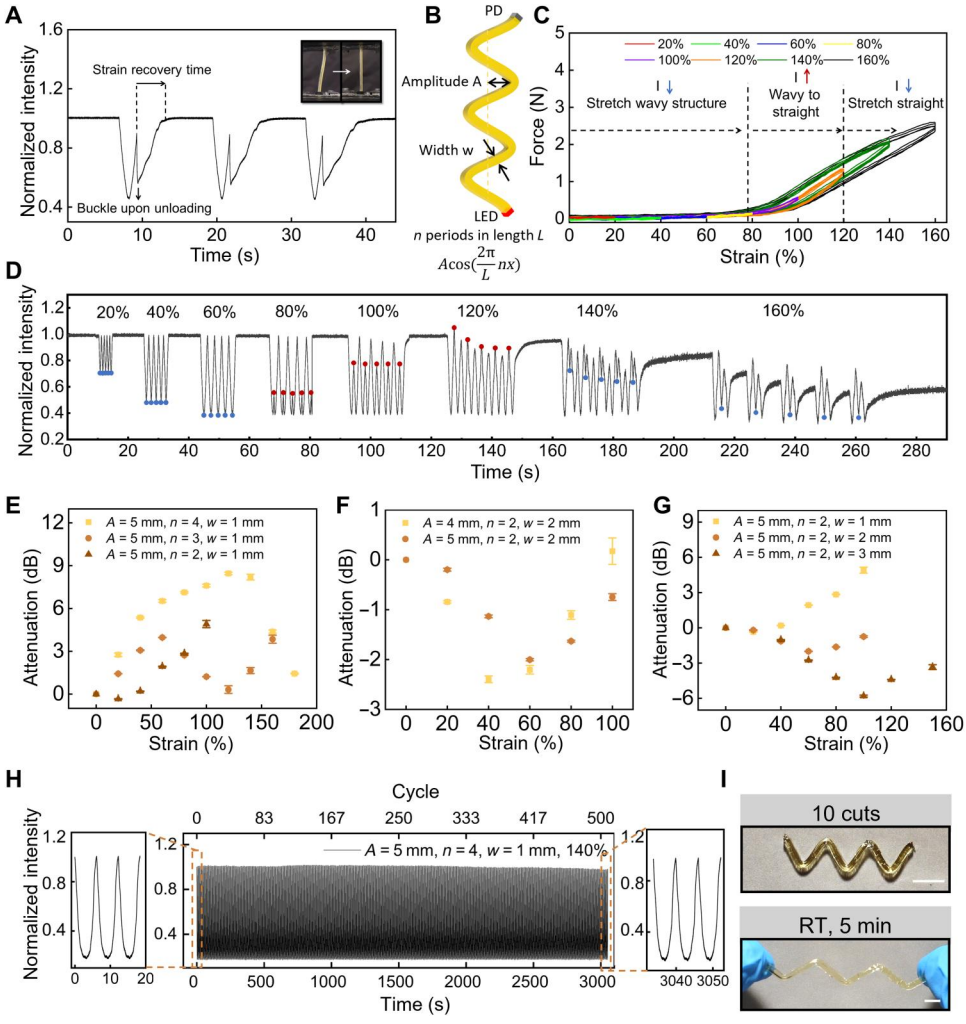

Fig. 3. Wavy sensor design to improve elasticity for dynamic strain sensing. (**A**) Realtime sensor response to three loading and unloading cycles to 60% strain. Inset: Photography of sensor buckling and strain recovery upon unloading due to material's viscoelasticity. (**B**) Schematics of wavy SHeaLDS with design variables. (**C** and **D**) Force versus strain response (C) and output intensity response (D) of cyclic tensile tests of a wavy sensor (A = 5 mm, n = 3, w = 1 mm) to different strains at 60 mm min^{-1}: ε < 140% strain each with five cycles and no strain recovery time in between cycles, and ε = 160% with 5-s recovery time. (**E** to **G**) Wavy sensor strain response with various sensor design parameters: period (E), amplitude (F), and width (G). (**H**). Cyclic test with 500 continuous cycles to ε = 140% shows no drift or hysteresis. Strain rates are 100 mm min^{-1}. (**I**). A wavy sensor (sPUU2000) with improved elasticity chopped into 10 pieces can resume stretching after self-healing at room temperature for 5 min (movie S4). Scale bars, 5 mm.

drift and hysteresis under continuous cyclic loadings (i.e., downshifting work loops and nonoverlapping loading and unloading curves; fig. S7); drift can be minimized given enough strain recovery time, subject to loading conditions (e.g., 20 s for ε_{max} = 30%), between each loading cycles (fig. S8). In either case, reliable dynamic strain sensing could not be achieved due to large hysteresis, limited strain range, and bandwidth.

To overcome sensing challenges from viscoelasticity while maintaining self-healing ability, we designed SHeaLDS into a wavy shape that exploits structural compliance. The wavy structure (Fig. 3B) accommodates strains with changes in amplitudes and periods, thus minimizing stress and strain on the self-healing material (*1*, *41*, *42*). As the wavy structure straightens, stress on the self-healing material at the peaks and troughs of the wave changes from minimal (i.e., force close to zero for ε < 120%) to more pronounced (ε > 120%; Fig. 3C); accordingly, dynamic strain sensing exhibits no hysteresis or drift for ε < 120% and increasing hysteresis and drift for ε > 120% (Fig. 3D). Thus, the elastic and nonhysteretic strain range for dynamic measurement can be characterized by the maximum strain that maintains minimal material stress (i.e., transition strain from wavy to straight structure).

Continuous cyclic loadings of a SHeaLDS (wave parameters: amplitude A = 5 mm, number of periods n = 3, and width w = 1 mm) shows three distinct output response phases to increasing strain (Fig. 3, C and D)—intensity decrease for ε < 78% (phase i), increase for 78% < ε < 120% (phase ii), and decrease for ε > 120% (phase iii). The intensity decrease in phase i is counterintuitive, because we expect the output intensity to monotonically increase due to the diminishing bending loss as the wavy sensor straightens. Ray optic simulation (COMSOL) reveals mechanisms behind this intensity decrease: Coupling alignment loss between the light-emitting diode (LED) and the waveguide becomes stronger with larger

strains as a result of the spatially fixed LED and coupler; bend loss at the wave peaks and troughs only starts to substantially recover when the bending angle further straightens beyond ~90° (fig. S9 and note S2). Thus, wave designs with undeformed peak angles close to or flatter than ~90° exhibits monotonic intensity increase when waves are straightened (n = 2; Fig. 3, E to G); more wavy designs with sharper peaks experience the two-phase response (n = 3 and 4; Fig. 3E). Larger wave amplitude (A) and more period numbers (n) boost the elastic and nonhysteretic strain range (Fig. 3, E and F); larger sensor width boosts this range as well, possibly due to the wider waveguide supporting more modes (Fig. 3G). SHeaLDS (A = 5 mm, n = 4, w = 1 mm) achieves reliable dynamic sensing to ε =140% with no hysteresis or drift in a continuous cyclic test with 500 cycles (Fig. 3H). A wavy sensor chopped into 10 pieces can resume stretching after self-healing at room temperature for 5 min (Fig. 3I and movie S4).

Self-healing and damage intelligent soft robots via SHeaLDS

Integrating SHeaLDS sensors (Fig. 4A, ii) with self-sealing soft actuators [i.e., fiber-silicone composite previously reported; Fig. 4A, ii and (*43*)] to enable feedback control, we demonstrate a damage intelligent soft quadruped with autonomous self-healing ability, awareness, and adaptability to severe damage (Fig. 4A, iv). In the first demonstration, we stabbed a leg of the quadruped with a sharp knife for multiple times and only allowed a few minutes for functional recovery at room temperature without any external stimuli. The intact leg first cyclically bends at 1 Hz with ΔP ~ 15-psi pressure, and the actuation is dynamically monitored with the sensor′s normalized output intensity oscillating between 1 and 0.8 (Fig. 4B). Our controller detects a stab when the normalized intensity decreases below 0.2, which triggers a halt in the actuation to allow self-healing for a certain time. The controller counts the number of stabs and increases the postdamage healing time for the first three stabs, mimicking the animal′s need for prolonged healing when injured more severely; from the fourth to sixth stab, the controller adjusts healing time to only 1 min, demonstrating the robot′s fast recovery abilities (Fig. 4B and movie S5). We increased actuation pressure after each stab to maintain similar level of actuation given air leakage; to boost extreme damage detection range, we increased the photodiode (PD)′s gain when motion sensing signal drops close to damage detection threshold from too many stabs (Fig. 4B). The robot shows the ability to maintain functionality (i.e., damage detection, motion sensing, actuation, and feedback control) close to the pristine state even after being damaged for six times. In the second demonstration, we used five SHeaLDS to monitor the gait and damage state of the quadruped and control the movement direction based on damage condition (Fig. 4C and movie S6). The robot first moves forward with an undulating gait that sequentially actuates the front legs, middle body, and back legs, and it then comes to a halt with all actuators inflated to wait for a cut. The injured leg is identified by the SHeaLDS with the most substantial intensity decrease compared to other legs, which is also reflected in the decreased normalized intensity baseline in the robot′s resting state (Fig. 4C). After detecting a cut, the robot rests for 3 min and then turns toward the opposite direction of the cut (right/left turn gait: back left/right leg and both front legs alternate with middle body inflated, all monitored in sensor signals). We made cuts on four legs and activated turning for four times to demonstrate the damage-based feedback control; the sensing signal remains intact and reflects gait and damage state despite the cuts; the robot′s mobility deteriorates due to the shared pressure source of the actuators, which could be solved by using one tunable pressure source for each actuator (note S3).

DISCUSSION

We have introduced SHeaLDS, an autonomously self-healing and damage-resilient stretchable optomechanical sensor that achieves hyperelastic strains (140%), resilient to large works of extension (60.6 MJ m^{-3}), and room temperature self-healing abilities, as well as reliable dynamic sensing performance to these large strains. Although ε ~ 100% self-healable strain of the material at room temperature is shown for our robotic demonstration, over ε > 1000% self-healable strain can be achieved with sPUU1000 at room temperature or sPUU2000 with heating for applications involving extreme deformations. Expediated healing could be achieved by heating (Fig. 1F). Distributed heating elements, such as resistive heating or photothermal heating through embedded nanoparticles, could be incorporated to achieve faster self-healing rates with onboard control.

We demonstrate a damage intelligent soft robot, enabled by SHeaLDS, that senses injury and self-heals from severe damage on the molecular level within minutes. For robotic applications, a limitation of the intrinsically self-healing scheme is the requirement for material contact to allow self-healing of mechanical strength. The environment robots operate in could introduce impurities, such as debris or chemicals, and when damage is incurred, surface fouling could prevent clean surfaces to contact and self-heal. Proper encapsulation, design, and extrinsic or a combination of extrinsic and intrinsic self-healing mechanisms may be necessary to address the demanding self-healing conditions in these applications. Damage intelligence realized through SHeaLDS demonstrates autonomy in damage sensing, healing, and adaptation resembling physical intelligence in animals. Combined with advances in artificial intelligence, SHeaLDS presents a route toward more enduring and adaptive robots. Beyond robotics, we envision SHeaLDS to find utility in the broader area where damage intelligence is essential in damage-prone environments, such spacesuits and supersonic parachute monitoring in space (*44*), as well as applications where device longevity is preferred, such as wearables for human machine interaction and digital health.

MATERIALS AND METHODS

Materials

PTMEG (M_n = 650 g mol^{-1}, M_n = 1000 g mol^{-1}, and M_n = 2000 g mol^{-1}), isophorone diisocyanate (IPDI; 98%), 1,4-diazabicyclo[2.2.2]octane (DABCO; 99%), *N*,*N*-dimethylacetamide (DMAc; 99.8%), and 4-aminophenyl disulfide (APDS; 98%) were purchased from Sigma-Aldrich and used without further purification.

sPUU synthesis

First, a *bis*-isocyanate–terminated PU prepolymer is obtained from the reaction of PTMEG (M_n = 650 g mol^{-1}, M_n = 1000 g mol^{-1}, and M_n = 2000 g mol^{-1}) as the soft segment and IPDI (98%) as the hard segment in the DMAc (99.8%) solution with DABCO (99%) as the catalyst at 70°C. The PU prepolymers are then linked

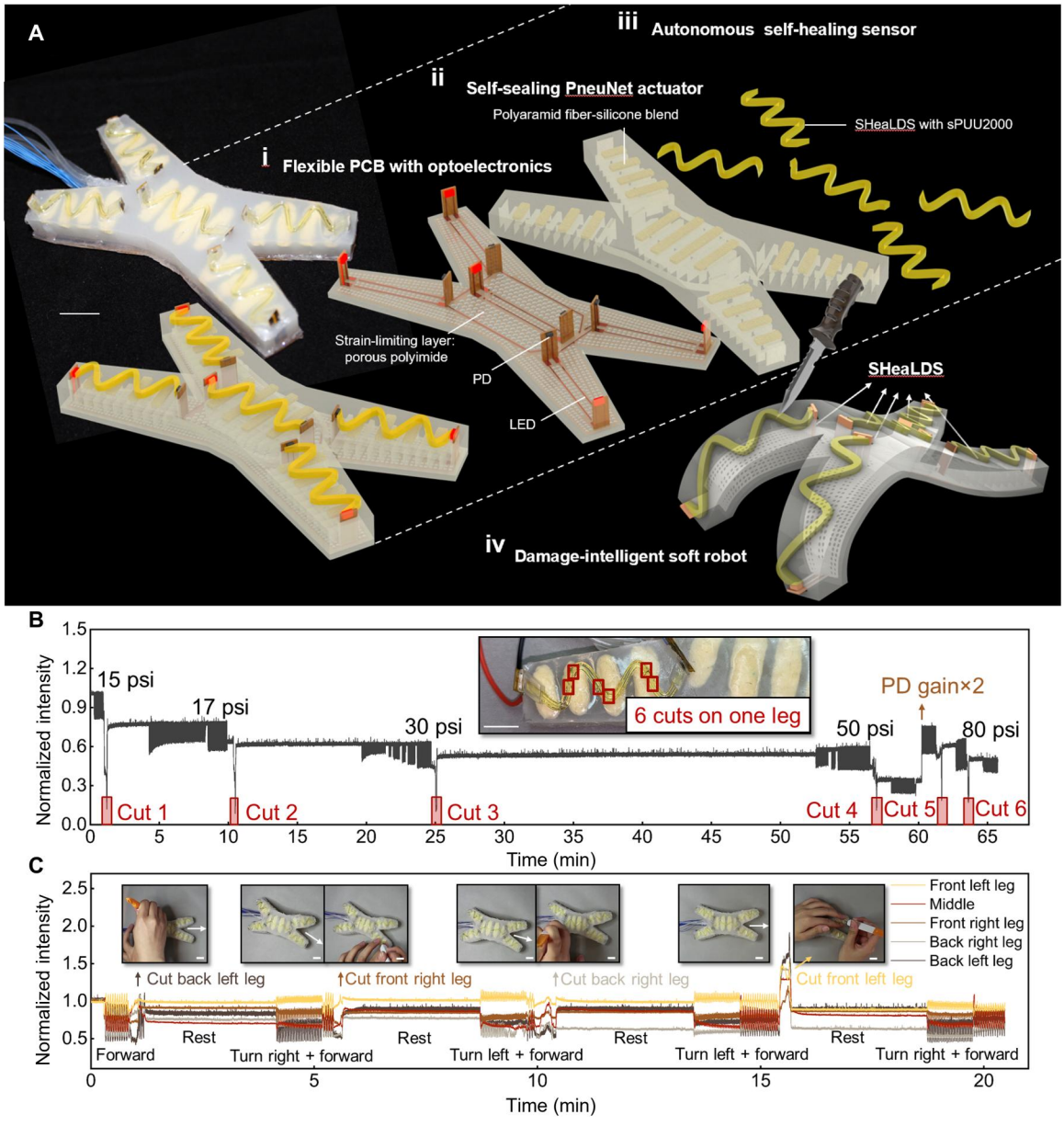

Fig. 4. Damage-aware and autonomously self-healable intelligent soft robot. (**A**) Schematic illustrations and photographs of the sPUU integrated pneumatic soft quadruped (iv) composed of a flexible PCB layer for optoelectronics routing and PN actuator strain limiting (i), self-sealing PN actuators (ii), and wavy optical waveguide sensors with sPUU2000 (iii). (A and C) Robot's autonomous adaptation to cuts with no external intervention via damage-detecting and self-healing sensors used for feedback control: (**B**) Adaptation of one leg subject to severe damages by controlling its actuation based on the number of cuts. (**C**) Gait adaptation as different legs are damaged to mimic the escape response of animals to danger. Scale bars, 1 cm.

with APDS as chain extenders with dynamic covalent bonds at 60°C. The mixture solidifies at 60°C in silicone molds (M 4601 Wacker) with cavities in the shape of optical waveguide designs, which are created via molding the silicones from three-dimensional (3D)–printed molds (VeroBlue, Objet). Last, residual solvent is removed by vacuum drying at 60°C.

Predehydrated PTMEG (0.0145 mol; 9.425 g for Mn = 650 g mol^{-1}, 14.5 g for Mn = 1000 g mol^{-1}, and 29 g for Mn = 2000 g mol^{-1}) was heated for 30 min in a dried round-bottom flask equipped with a mechanical stirrer in an oil bath at 70°C under an argon environment. IPDI (6.77 g, 0.03045 mol) and DABCO [3 weight % (wt %)] were dissolved in DMAc (10 ml) and added dropwise to PTMEG to react at 70°C with stirring in the argon environment (1.5 hours for Mn = 650 g $mol^{-1}$and Mn = 1000 g mol^{-1} and 7.5 hours for Mn = 2000 g mol^{-1}). After the mixture was cooled to room temperature, APDS (3.6 g, 0.0145 mol) dissolved in DMAc (20 ml) was added dropwise to the PU prepolymer and heated to 60°C with stirring for 1.5 hours. The reaction time was checked by Fourier transform infrared spectroscopy by observing the decrease of the isocyanate stretching band at 2264 cm^{-1} (fig. S10). The mixture was then poured into silicone molds (ELASTOSIL M 4601 A/B, Wacker Chemie AG) preheated to 60°C and heated at

60°C on a hot plate for 24 hours. Residual solvent was further removed by vacuum drying at 60°C for 12 hours. No bubbles were observed in the sPUU products.

Material characterization

The two-step sPUU synthesis was monitored by Fourier transform infrared spectroscopy (Nicolet iz10, Thermo Fisher Scientific) where the reaction time for steps one and two was determined by the time for no further decrease of the isocyanate peak in each step (fig. S10). The number-averaged molecular weight (M_n), weight-averaged molecular weight (M_w), and PDI were measured by gel permeation chromatography (GPC) (Waters Ambient Temperature GPC: Tetrahydrofuran) with narrow polystyrene standards. As the molecular weight of PTMEG increased, the product's molecular weight (M_n) increased from 17 to 62 kDa and showed narrow molecular weight distribution with PDI in the range of 1.49 to 1.65 (table S2).

Tensile tests comparing mechanical properties of sPUU650, sPUU1000, and sPUU2000 (Fig. 1B) were performed on Instron 5566 at 100 mm min^{-1}; tensile tests for the sPUU1000 self-healing characterization (Fig. 1C) were performed on Zwick-Roell Z010 tester at 60 mm/min; tensile tests for the sPUU2000 self-healing characterization (Fig. 1D) were performed on Instron 5566 at 500 mm/min. Variations in testing conditions were due to the difficult laboratory availabilities during coronavirus disease 2019 (COVID-19). Tensile test results show that as the soft segment becomes longer, the sPUU becomes softer due to decreased cross-linking density: sPUU650 is stiff with tangent modulus E = 43.6 MPa at $0 < \varepsilon < 0.1$, sPUU1000 is softer with E = 4.12 MPa at $0 < \varepsilon < 0.15$, and sPUU2000 is the softest with E = 1.3 MPa at $0 < \varepsilon < 0.3$. The fracture strain of sPUU650 is $\varepsilon \sim$ 500%, whereas those of sPUU1000 and sPUU 2000 are $\varepsilon >$ 1000%.

Viscoelastic properties of the sPUU were characterized by extensional storage and loss modulus measurements and creep tests via dynamic mechanical analysis (DMA) (TA Instruments, DMA Q800). The extensional storage and loss modulus measurements were performed with imposed oscillations of a 0.5-MPa maximum stress (in the elastic region of all samples), at a 1-Hz frequency, and with a temperature sweep from −100° to 100°C at a rate of 3°C/min. As shown in table S1 and fig. S2, the glass transition temperatures, taken as temperature at the maximum loss modulus, increased as the PTMEG molecular weight decreased. At 25°C, sPUU2000 and sPUU1000 were in the rubbery state, while sPUU 650 was in the glassy state. Single-step creep tests for sPUU 650, sPUU 1000, and sPUU 2000 were performed at 25°C with a preload of 0.001 N and a prescribed stress of 0.1 MPa for 1 min (fig. S3). sPUU 2000 fully recovered the $\varepsilon \sim$ 10% deformed strain in 6 min; sPUU 1000 fully recovered the $\varepsilon \sim$ 2.5% deformed strain in 11 min; sPUU 650 could not recover the strain. sPUU 650 is eliminated from our material selection for the stretchable sensor. Thermal property was also characterized by thermal gravimetric analysis (Instrument Q500). sPUU 2000 showed 5% weight loss at 327°C (fig. S11).

Optical properties were characterized by ultraviolet-visible/near-infrared (NIR) spectrophotometry (Cary 5000) and ellipsometry. Transmissions of 1.5-mm-thick sPUU650, sPUU1000, and sPUU2000 samples were measured to be greater than 80% in red and NIR wavelengths (Fig. 2A). The refractive index of sPUU2000 was obtained by Woollam Spectroscopic Ellipsometer with data fitted to the Cauchy model. sPUU 2000 had a refractive index (n) of more than 1.5 in the red and NIR wavelengths (fig. S12), greater than those of many commercially available silicone elastomers [$n < 1.45$; (*37*, *39*)] for these wavelengths, making sPUU2000 readily integrable as the optical fiber core material in intrinsically soft actuators and sensors.

Waveguide fabrication

Optical waveguides were fabricated via replica molding and were coupled with a NIR LED chip (15412085A9000, Würth Elektronik) to one end and an infrared PD chip (SFH 2700 FA, OSRAM Opto Semiconductors) to the other end. sPUUs were poured into heated silicone molds (60°C) with cavities of different waveguide designs for curing with procedures as described above. Straight waveguides had the dimension of 3.2 mm by 1.5 mm by 7 cm, and wavy waveguides were 4-cm long and 2-mm thick with various amplitude (A = 5 or 4 mm), period (n = 2, 3, or 4), and width (w = 1, 2, or 3 mm) as shown in Fig. 3B. The silicone molds were obtained by molding from 3D-printed rigid molds (VeroBlue, glossy surface finish, Objet 30, Stratasys Ltd.) with the waveguide designs. The 3D-printed molds were first heated to 80°C for 6 hours to remove residual resin, and then, the mixture of M 4601 parts A and B (9:1 by weight) were poured into the molds and heated to 80°C for 1 hour to cure.

COMSOL ray optics simulation

We performed simulation to understand the counterintuitive wavy sensor's response to small elongations (phase i), where the output intensity decreased with decreasing curvatures. Ray optics simulation was selected because the sensor's cross-sectional dimension was much larger than NIR wavelengths. A wavy sensor with A = 5 mm, n = 4 periods with a length of 40 mm, w = 1 mm, and thickness = 2 mm was simulated in COMSOL ray optics module. sPUU2000 was modeled as linear elastic material with Young's modulus of 1.3 MPa and Poisson's ratio of 0.44, because the force versus strain response of the wavy sensor (Fig. 3C) suggested that the initial elongations contributed to mostly structural deformation instead of material's deformation. The refractive index was set as 1.52, and the sensor was surrounded by air. Light source was modeled to be released from boundary (the LED coupling input surface) with 100 rays per release, conical ray director vector with uniform density, and 50 rays in wave vector space. The cone axis was set tangent to the cosine curve with a cone axis of pi/24 rad. Output intensity was collected by a ray detector at the PD coupling output surface. The LED coupling input surface was set as a fixed boundary simulating the LED-waveguide coupling fixture. The PD coupling output surface was prescribed horizontal displacements. Experimental and theoretical results with the same wavy sensor parameters show similar three-phase increase-decrease-increase output intensity attenuation response to elongation with comparable strain cutoffs (fig. S9). The attenuation difference in phase ii was due to the absence of material absorbance modeling in the simulation, indicating a larger output intensity in the straight waveguide schematic. For the purpose of understanding the phase i response, however, the model provides good validation and explanation (fig. S9).

Robot fabrication

We integrated wavy SHeaLDS into a self-sealing soft quadruped to monitor motion and detect damage for feedback control. The

quadruped's architecture (Fig. 4A) is based on a multigait soft robot described previously (*45*), where five pneumatic actuators with PneuNet (PN) (*46*) channels can be sequentially modulated to allow mobility with multiple gaits and in different directions (*5*, *45*). Molds for the PNs were first 3D-printed (VeroBlue, glossy surface finish, Objet 30, Stratasys Ltd.) and baked at 80°C for 6 hour to remove residual resin. PNs were then molded with silicone elastomer (Ecoflex 00-20, Smooth-on Inc.) to a total height of 6 mm with the pneumatic channel height at 4 mm (fig. S13) and cured for 20 min at 80°C.

To make the PN actuators also damage resilient, we adopted a self-sealing design previously reported (*43*), where a silicone-polyaramid fiber composite enabled soft pneumatic actuators to be puncture resilient through the combination of self-adhesion from silicones and mitigation of crack propagation from fibers. Polyaramid fibers (15 wt %; Kevlar Pulp, FibreGlast Inc.) were blended with uncured silicone matrix (85 wt %; Ecoflex 00-20, Smooth-on Inc.) that produced paste-like composites. The composites were formed in the shape of rectangular islands and placed on top of the cured PNs. Uncured silicone resin (Ecoflex 00-20, Smooth-on Inc.) was poured to fill the space in between the fiber composite islands and bond the fiber composites with the PNs. Each of the five pneumatic chambers was connected to a soft silicone tubing (outer diameter of 1.27 mm; Silastic Laboratory Tubing, Dow Corning) routed and glue-fixed (Sil-Poxy, Smooth-On Inc.) into a hub located at the rear of the robot (fig. S13). Pneumatic channels of the PNs were sealed by first bonding to a thin layer (0.5 mm, screen printed) of uncured clear silicone elastomer (ELASTOSIL RT 625 A/B, Wacker Chemie AG) and baked at 80°C for 2 hours to cure.

One SHeaLDS with sPUU2000 and the wavy design A = 5 mm, n = 3, and w = 1.6 mm (Fig. 4D) is integrated on top of each PN actuator and coupled to an LED (15412085A9000, Würth Elektronik) on one end and a PD (SFH 2700 FA, OSRAM Opto Semiconductors) on the other. The optoelectronics are embedded via a flexible printed circuit board (Flex PCB) design (Fig. 4B and fig. S14), where the LEDs and PDs are soldered on Flex PCBs that are vertically connected to a mainboard (via soldering) for electrical routing. The mainboard is punctured with holes to also function as the strain-limiting layer for the PN actuator, which translates the uniform pressurization to anisotropic bending motions.

SHeaLDS were connected to the optoelectronics at the top of the robot assembly via 3D- printed connectors (LOCTITE 3D IND405 Clear, Carbon M1). The optoelectronics were secured to the robot's silicone body by gluing (LOCTITE Super Glue) the flexible PCBs to the peripheral silicone; the 3D-printed connectors were aligned with and secured to the optoelectronics by gluing the connectors with the flexible PCBs; the sPUU waveguide sensors were press-fitted to the connectors for alignment with the optoelectronics. Last, a thin layer (0.5 mm) of silicone adhesive (Sil-Poxy, Smooth-On Inc.) was brushed onto the side walls of the robot for stiffening, so that pressure was directed to stretch the top layers and produce bending motions. Figure S17 shows a fully assembled soft quadruped with SHeaLDS.

Robot control

The five actuators shared one pressurized air source, and each actuator was connected to a pair of solenoid valves (X-Valve, Parker Hannifin) that were both normally closed (fig. S15). Opening the inflating valve while closing the deflating valve inflated the actuator, closing both valves held the inflation, and closing the inflating valve while opening the deflating valve deflated the actuator. We collected output intensities from the five waveguide sensors through PDs with various amplifying gains (fig. S16) due to variations in the waveguide fabrication and integration. We fed back the sensor signal of damage detection to control the robot's actuation. In the first demonstration, as we cut one leg six times, the controller autonomously adjusted robot's resting time based on the number of times the leg had been cut. In this case, a decrease of the normalized intensity past the 0.2 threshold triggers the damage detection. Note that in movie S5, there are random spikes in the signal due to unstable connection of a wire that may be confused with the cut signal. The controller filters out this effect by setting a time threshold that differentiates a fast spike from a cut. We changed the input pressure and the operational amplifier p gain manually in this demonstration instead of setting up an analog pressure source and the metal–oxide–semiconductor field-effect transistor (MOSFET) controlled gain, because of pandemic-related time and resource constraints. These two parameters could be changed via the controller automatically if integrated as described above. In the second demonstration, we control the gait of the robot to change its movement direction as the four legs were cut, mimicking the escape behavior of animals when facing danger. Because the waveguide sensor material (sPUU2000) was very tough, it was difficult to cut the waveguide with a sharp blade when the tough sensor sat on the soft silicone PN. To increase the rigidity of the sensor substrate and allow the knife to fully penetrate the top layers, we inflate all five pneumatic chambers with a button input before cutting one of the legs. We expect the cut detection to be similar to the first demonstration where the cut was signaled by an intensity decrease past a threshold. In this demonstration, however, the LEDs and PDs were slightly up-facing coupled, instead of level coupled, to the waveguide due to soldering positions, rendering the waveguide into a proximity sensor. As the hand approached the robot from the top to make a cut, the sensor signals increased; as a cut was made, the corresponding sensor had a slight intensity decrease, because the PD was receiving both the light propagating in the waveguide only and the light reflected from the hand and coupled into the waveguide. We adjusted the cut detection to a prolonged increase in any of the sensor signal from the four legs to indicate hand approaching, followed by detecting the most substantial intensity decrease among the uncut legs to identify which leg was cut.

Supplementary Materials

This PDF file includes:
Supplementary Text
Figs. S1 to S18
Tables S1 and S2

Other Supplementary Material for this manuscript includes the following:
Movies S1 to S6

REFERENCES AND NOTES

1. J. A. Rogers, T. Someya, Y. Huang, Materials and mechanics for stretchable electronics. *Science* **327**, 1603–1607 (2010).
2. M. L. Hammock, A. Chortos, B. C.-K. Tee, J. B.-H. Tok, Z. Bao, 25th anniversary article: The evolution of electronic skin (E-Skin): A brief history, design considerations, and recent progress. *Adv. Mater.* **25**, 5997–6038 (2013).

3. M. Amjadi, K. U. Kyung, I. Park, M. Sitti, Stretchable, skin-mountable, and wearable strain sensors and their potential applications: A review. *Adv. Funct. Mater.* **26**, 1678–1698 (2016).
4. S. Li, H. Bai, R. F. Shepherd, H. Zhao, Bio-inspired design and additive manufacturing of soft materials, machines, robots, and haptic interfaces. *Angew. Chemie Int. Ed. Engl.* **58**, 11182–11204 (2019).
5. M. T. Tolley, R. F. Shepherd, B. Mosadegh, K. C. Galloway, M. Wehner, M. Karpelson, R. J. Wood, G. M. Whitesides, A resilient, untethered soft robot. *Soft Robot.* **1**, 213–223 (2014).
6. P. Polygerinos, N. Correll, S. A. Morin, B. Mosadegh, C. D. Onal, K. Petersen, M. Cianchetti, M. T. Tolley, R. F. Shepherd, Soft robotics: Review of fluid-driven intrinsically soft devices; Manufacturing, sensing, control, and applications in human-robot interaction. *Adv. Eng. Mater.* **19**, 1700016 (2017).
7. R. Adam Bilodeau, R. K. Kramer, Self-healing and damage resilience for soft robotics: A review. *Front. Robot. AI.* **4**, 48 (2017).
8. Y. Chen, H. Zhao, J. Mao, P. Chirarattananon, E. F. Helbling, N.-S. P. Hyun, D. R. Clarke, R. J. Wood, Controlled flight of a microrobot powered by soft artificial muscles. *Nature* **575**, 324–329 (2019).
9. L. Kluis, N. Keller, H. Bai, N. Iyengar, R. Shepherd, A. Diaz-Artiles, Reducing metabolic cost during planetary ambulation using robotic actuation. *J. Aerosp. Med. Hum. Perform.* **92**, 570–578 (2021).
10. S. Terryn, J. Brancart, D. Lefeber, G. Van Assche, B. Vanderborght, Self-healing soft pneumatic robots. *Sci. Robot.* **2**, eaan4268 (2017).
11. S. K. Tabrizian, F. Sahraeeazartamar, J. Brancart, E. Roels, P. Ferrentino, J. Legrand, G. Van Assche, B. Vanderborght, S. Terryn, A healable resistive heater as a stimuli-providing system in self-healing soft robots. *IEEE Robot. Autom. Lett.* **7**, 4574–4581 (2022).
12. S. Terryn, J. Langenbach, E. Roels, J. Brancart, C. Bakkali-Hassani, Q.-A. Poutrel, A. Georgopoulou, T. George Thuruthel, A. Safaei, P. Ferrentino, T. Sebastian, S. Norvez, F. Iida, A. W. Bosman, F. Tournilhac, F. Clemens, G. Van Assche, B. Vanderborght, A review on self-healing polymers for soft robotics. *Mater. Today* **47**, 187–205 (2021).
13. E. J. Markvicka, M. D. Bartlett, X. Huang, C. Majidi, An autonomously electrically self-healing liquid metal-elastomer composite for robust soft-matter robotics and electronics. *Nat. Mater.* **17**, 618–624 (2018).
14. S. R. White, N. R. Sottos, P. H. Geubelle, J. S. Moore, M. R. Kessler, S. R. Sriram, E. N. Brown, S. Viswanathan, Autonomic healing of polymer composites. *Nature* **409**, 794–797 (2001).
15. C. J. Hansen, W. Wu, K. S. Toohey, N. R. Sottos, S. R. White, J. A. Lewis, Self-healing materials with interpenetrating microvascular networks. *Adv. Mater.* **21**, 4143–4147 (2009).
16. B. J. Blaiszik, S. L. B. Kramer, S. C. Olugebefola, J. S. Moore, N. R. Sottos, S. R. White, Self-healing polymers and composites. *Annu. Rev. Mat. Res.* **40**, 179–211 (2010).
17. S. Wang, M. W. Urban, Self-healing polymers. *Nat. Rev. Mater.* **5**, 562–583 (2020).
18. J. F. Patrick, M. J. Robb, N. R. Sottos, J. S. Moore, S. R. White, Polymers with autonomous life-cycle control. *Nature* **540**, 363–370 (2016).
19. A. Pena-Francesch, H. Jung, M. C. Demirel, M. Sitti, Biosynthetic self-healing materials for soft machines. *Nat. Mater.* **19**, 1230–1235 (2020).
20. B. C.-K. Tee, C. Wang, R. Allen, Z. Bao, An electrically and mechanically self-healing composite with pressure- and flexion-sensitive properties for electronic skin applications. *Nat. Nanotechnol.* **7**, 825–832 (2012).
21. L. M. Zhang, Y. He, S. Cheng, H. Sheng, K. Dai, W. J. Zheng, M. X. Wang, Z. S. Chen, Y. M. Chen, Z. Suo, Self-healing, adhesive, and highly stretchable ionogel as a strain sensor for extremely large deformation. *Small* **15**, 1804651 (2019).
22. D. Hardman, T. George Thuruthel, F. Iida, Self-healing ionic gelatin/glycerol hydrogels for strain sensing applications. *NPG Asia Mater.* **14**, 11 (2022).
23. Q. Zhang, S. Niu, L. Wang, J. Lopez, S. Chen, Y. Cai, R. Du, Y. Liu, J.-C. Lai, L. Liu, C.-H. Li, X. Yan, C. Liu, J. B.-H. Tok, X. Jia, Z. Bao, An elastic autonomous self-healing capacitive sensor based on a dynamic dual crosslinked chemical system. *Adv. Mater.* **30**, 1801435 (2018).
24. M. Khatib, O. Zohar, H. Haick, Self-healing soft sensors: From material design to implementation. *Adv. Mater.* **33**, 2004190 (2021).
25. J. Kang, J. B.-H. Tok, Z. Bao, Self-healing soft electronics. *Nat. Electron.* **2**, 144–150 (2019).
26. Y. Chen, A. M. Kushner, G. A. Williams, Z. Guan, Multiphase design of autonomic self-healing thermoplastic elastomers. *Nat. Chem.* **4**, 467–472 (2012).
27. J. Kang, D. Son, G.-J. N. Wang, Y. Liu, J. Lopez, Y. Kim, J. Y. Oh, T. Katsumata, J. Mun, Y. Lee, L. Jin, J. B.-H. Tok, Z. Bao, Tough and water-insensitive self-healing elastomer for robust electronic skin. *Adv. Mater.* **30**, 1706846 (2018).
28. S.-M. Kim, H. Jeon, S.-H. Shin, S.-A. Park, J. Jegal, S. Y. Hwang, D. X. Oh, J. Park, Superior toughness and fast self-healing at room temperature engineered by transparent elastomers. *Adv. Mater.* **30**, 1705145 (2018).
29. H. Guo, Y. Han, W. Zhao, J. Yang, L. Zhang, Universally autonomous self-healing elastomer with high stretchability. *Nat. Commun.* **11**, 2037 (2020).
30. J. M. Matxain, J. M. Asua, F. Ruipérez, Design of new disulfide-based organic compounds for the improvement of self-healing materials. *Phys. Chem. Chem. Phys.* **18**, 1758–1770 (2016).
31. E. Formoso, J. M. Asua, J. M. Matxain, F. Ruipérez, The role of non-covalent interactions in the self-healing mechanism of disulfide-based polymers. *Phys. Chem. Chem. Phys.* **19**, 18461–18470 (2017).
32. I. Azcune, I. Odriozola, Aromatic disulfide crosslinks in polymer systems: Self-healing, reprocessability, recyclability and more. *Eur. Polym. J.* **84**, 147–160 (2016).
33. Y. H. Kim, R. P. Wool, A theory of healing at a polymer-polymer interface. *Macromolecules* **16**, 1115–1120 (1983).
34. J. Zheng, Z. M. Png, S. H. Ng, G. X. Tham, E. Ye, S. S. Goh, X. J. Loh, Z. Li, Vitrimers: Current research trends and their emerging applications. *Mater. Today* **51**, 586–625 (2021).
35. P. Cordier, F. Tournilhac, C. Soulié-Ziakovic, L. Leibler, Self-healing and thermoreversible rubber from supramolecular assembly. *Nature* **451**, 977–980 (2008).
36. M. Arisawa, A. Suwa, M. Yamaguchi, $RhCl_3$-catalyzed disulfide exchange reaction using water solvent in homogeneous and heterogeneous systems. *J. Organomet. Chem.* **691**, 1159–1168 (2006).
37. H. Zhao, K. O'Brien, S. Li, R. F. Shepherd, Optoelectronically innervated soft prosthetic hand via stretchable optical waveguides. *Sci. Robot.* **1**, eaai7529 (2016).
38. P. A. Xu, A. K. Mishra, H. Bai, C. A. Aubin, L. Zullo, R. F. Shepherd, Optical lace for synthetic afferent neural networks. *Sci. Robot.* **4**, eaaw6304 (2019).
39. H. Bai, S. Li, J. Barreiros, Y. Tu, C. R. Pollock, R. F. Shepherd, Stretchable distributed fiber-optic sensors. *Science* **370**, 848–852 (2020).
40. J. C. Palais, *Fiber Optic Communications* (Prentice Hall, 1998), 342 pp.
41. D.-H. Kim, J.-H. Ahn, W. M. Choi, H.-S. Kim, T.-H. Kim, J. Song, Y. Y. Huang, Z. Liu, C. Lu, J. A. Rogers, Stretchable and foldable silicon integrated circuits. *Science* **320**, 507–511 (2008).
42. D.-Y. Khang, H. Jiang, Y. Huang, J. A. Rogers, A stretchable form of single-crystal silicon for high-performance electronics on rubber substrates. *Science* **311**, 208–212 (2006).
43. R. F. Shepherd, A. A. Stokes, R. M. D. Nunes, G. M. Whitesides, Soft machines that are resistant to puncture and that self seal. *Adv. Mater.* **25**, 6709–6713 (2013).
44. J. Jo, A. Xu, A. K. Mishra, H. Bai, A. Derkevorkian, J. Rabinovitch, H. Park, R. F. Shepherd, Measurement of parachute canopy textile deformation using mechanically invisible stretchable lightguides. *Adv. Mater. Technol.* , 2200437 (2022).
45. R. F. Shepherd, F. Ilievski, W. Choi, S. A. Morin, A. A. Stokes, A. D. Mazzeo, X. Chen, M. Wang, G. M. Whitesides, Multigait soft robot. *Proc. Natl. Acad. Sci.* **108**, 20400–20403 (2011).
46. F. Ilievski, A. D. Mazzeo, R. F. Shepherd, X. Chen, G. M. Whitesides, Soft robotics for chemists. *Angew. Chemie. Int. Ed. Engl.* **123**, 1930–1935 (2011).

Acknowledgments: We thank X. Liu for discussions about material synthesis, S. Li for suggestions about manuscript editing, A. M. Condo Jr. for performing GPC testing, and J. Yin from Cornell Energy Systems Institute for assistance with Fourier transform infrared spectroscopy testing, differential scanning calorimetry testing, and thermogravimetric analysis. **Funding:** This work was supported by the Air Force Office of Scientific Research (grant FA9550-18-1-0243), the NASA Innovative and Advanced Concepts program (grant number 80NSSC19K0969), and the NSF EFRI program (grant EFMA-1830924). Part of the study was performed at the Cornell NanoScale Facility, a member of the National Nanotechnology Coordinated Infrastructure, which was supported by the NSF (grant NNCI-1542081); at the Cornell Center for Materials Research Shared Facilities, which was supported through the NSF MRSEC program (grant DMR-1719875); and at the Cornell Energy Systems Institute. **Author contributions:** Concept, design, and study direction: H.B. and R.F.S. Material and sensor design: H.B. and R.F.S. Experimental validation: H.B. and Y.S.K. Robot design and fabrication: H.B., Y.S.K., and R.F.S. Theoretical modeling: H.B. Manuscript writing: H.B. and R.F.S. Manuscript editing: H.B., Y.S.K., and R.F.S. Supervision: R.F.S. Project administration: R.F.S. **Competing interests:** The authors declare that they have no competing interests. **Data and materials availability:** All data needed to evaluate the conclusions in the paper are present in the paper and/or the Supplementary Materials.

Submitted 24 March 2022
Accepted 1 November 2022
Published 7 December 2022
10.1126/sciadv.abq2104

Science Advances

Autonomous self-healing optical sensors for damage intelligent soft-bodied systems

Hedan BaiYoung Seong KimRobert F. Shepherd

Sci. Adv., 8 (49), eabq2104. • DOI: 10.1126/sciadv.abq2104